Hindawi Publishing Corporation
Mathematical Problems in Engineering
Volume 2016, Article ID 1409872, 13 pages
http://dx.doi.org/10.1155/2016/1409872

Research Article

High-Speed X-Ray Transmission and Numerical Study of Melt Flows inside the Molten Pool during Laser Welding of Aluminum Alloy

Jin Peng,[1] Liqun Li,[1] Shangyang Lin,[1,2] Furong Zhang,[1] Qinglong Pan,[3] and Seiji Katayama[3]

[1]*State Key Laboratory of Advanced Welding and Joining, Harbin Institute of Technology, Harbin, Heilongjiang 150001, China*
[2]*Harbin Welding Institute, Harbin, Heilongjiang 150080, China*
[3]*Joining and Welding Research Institute (JWRI), Osaka University, 11-1 Mihogaoka, Ibaraki, Osaka 567-0047, Japan*

Correspondence should be addressed to Jin Peng; pengjin1985120@163.com

Received 27 February 2016; Revised 9 June 2016; Accepted 15 June 2016

Academic Editor: Mohsen Asle Zaeem

By using the X-ray transmission imaging system, melt flows inside a molten pool were studied during laser welding of aluminum alloy at different welding speeds. Then, the correlation between temperature gradients along the direction of weld penetration and melt flows in the rear part of a molten pool was analyzed by using a three-dimensional numerical method. And the presented model was verified by experimental results. The corresponding investigation was carried out to further study the correlation between temperature gradient and melt flow behavior of the molten pool in the plate heated by preheating temperature. The results indicated that, in the rear part of the molten pool, the maximum flow velocity was located at the bottom of the molten pool. The melt metal in the rear molten pool caused by different welding speeds had significantly different flow trends. As the welding speed increased, the absorbed intensity on the keyhole front wall also increased as well as the recoil pressure that could maintain the keyhole opened. Consequently, the increase of the welding speed was more beneficial to improving the stability of the molten pool.

1. Introduction

Laser welding of aluminum alloys has been widely used in different industrial applications such as aerospace and vehicles because of its high productivity and low thermal input [1, 2]. However, the complexity of the aluminum laser welding process induces a number of weld defects such as pore formation, undercutting, underfilling, and solidification cracking [3]. It has been found that molten pool movements have a large influence on the creation of weld defects.

Many previous research works focused on molten metal flow based on experimental approaches and numerical simulations for improving the welding stability and process efficiency. The typical experimental results have been drawn from Osaka University by using the high-speed camera and the X-ray transmission imaging system [4]. Katayama and Matsunawa [5] studied the porosity formation and prevention mechanism during high-power CO_2 laser welding and YAG laser welding and found that many bubbles were intermittently formed mainly from the bottom tip of the keyhole. Some bubbles floated up and disappeared from the top surface and the amount of porosity was reduced, while others were captured at the solidifying front in the rear part of the molten pool, resulting in the formation of pores. Lots of bubbles could not disappear from the surface at a moderate speed, and as a result the porosity was high. Matsunawa [6] reported that the low viscosity of the aluminum melt promoted highly dynamical processes of molten pool. Kawahito et al. [7, 8] experimentally studied high-power fiber laser welding phenomena of stainless steel. The authors found that the melt flow was from the top to the bottom around the keyhole and from the bottom near the keyhole tip to the rear-bottom surface near the solidifying front at the low welding speeds, which was different from those at the high welding speeds. Li et al. [9] investigated the spatter formation and the molten pool behavior by using

the X-ray transmission imaging system of Osaka University. They reported that the recoil pressure of vapor on the keyhole wall was changed by different focal positions, and it could lead to different flow trends of molten metal on the keyhole wall. Thus, the whole flow trends of the molten pool could be changed and the spatter formation was changed. Meng et al. [10] observed the keyhole and molten pool dynamic behavior of high-strength low alloy in laser lap welding T-joints. When the gap increased, the direction and frequency of molten pool flows changed and a large number of bubbles were formed from the bottom tip of the keyhole.

For the sake of expensive experimental analysis and time consuming, quite few works have been conducted on the molten pool flow of laser welding by numerical simulation. Chang et al. [11] found that vortex was negative influence for stability of the molten pool, and a porosity formation mechanism could exist resulting from the onset of turbulent fluid flow behind the keyhole. Sohail et al. [12] studied weld pool behavior of 20 mm thick steel plate by using volume-of-fluid (VOF) method and found that, for higher laser power, a vortex was present, while, for 6 kW, such a vortex was not observed. Wang et al. [13] built a mathematical model considering keyhole formation and fluid flow in molten pool of titanium alloy. It was found that eddies were formed near the top and bottom surfaces of the molten pool, and larger fluid flow velocity occurred in the vicinity of the heat source location. In order to improve the stability of the molten pool, Zhang et al. [14] has developed numerical model of the transient behavior of molten pool and keyhole for full penetration laser welding of titanium alloy amd also found that appropriate control of a side gas flow jet acting on molten pool could alter the flow pattern in the molten pool and improve the stability of the molten pool, thereby reducing spatters and pores. Bachmann et al. [15] proposed the application of a magnetic field that could also reduce the fluid flow in the molten pool and prevent evolution of spatter and melt ejections. Furthermore, some research works have been undertaken to investigate regarding influence of driving forces on weld pool dynamics. Zhang et al. [16] achieved a computational analysis of full penetration laser welding and found that the lower surface of molten pool was more unstable than the upper surface of the molten pool. Recoil pressure and surface tension could be considered as the most dominant force for the transient flow field of the molten pool. Abderrazak et al. [17] found that the negative Marangoni effect in the magnesium alloy composition enhanced the heat transfer in the molten pool by driving melt flows, making the molten pool shape wider and shallower.

As mentioned above, the melt flow of molten pool was studied by a large number of researchers. The influence of process parameters on the molten pool dynamics in laser welding was analyzed. However, the correlation between temperature gradient along the direction of weld penetration and melt flow of molten pool in laser welding still remained unclear completely, especially in laser welding of aluminum alloy with highly dynamical processes. And the melt flows inside the molten pool were responsible for the stability of the molten pool, and even affected bubbles escape from the molten pool and distribution of alloying elements. Therefore, it is needed to further analyze the complicated physical processes. In this paper, melt flows inside the molten pool depending upon the welding speeds were investigated by using experimental and numerical simulation methods. Then, the relationship between temperature gradient along the direction of weld penetration and melt flows in the rear part of the molten pool was analyzed. The corresponding investigation was carried out to further study the correlation between the temperature gradient and the melt flow behavior inside the molten pool heated by the preheating temperature.

2. Experimental Setup

The Trumpf TurDisk-16002 laser equipment with a maximum power of 16 kW and a 280 mm focal length was used for welding experiment. The focus diameter was 0.28 mm. The materials used were 6056 aluminum alloy of 4 mm in plate thickness. The melt flow inside the molten pool during laser welding was observed through X-ray transmission real-time imaging apparatus. The system was schematically represented in Figure 1. The system consisted of a microfocused X-ray tube (150 kV, 900 mA) and an image converter, an image intensifier which could transform the X-ray transmission image to a visual image. The X-ray transmitted specimen was finally taken by the camera at a frame rate of 1000 f/s. The tungsten (W) particles of 100–300 μm in diameter were used to display the melt flow inside the molten pool. The other high-speed camera (Optronis GmbH, Germany, frame rate: 5000 f/s) was used to take the images of molten pool surface on the upper side. A filter (wavelength: 808 nm) and an illuminating laser (FC-W-808, Cavitar Ltd., Finland, wavelength: 808 nm) were introduced, accompanying the high-speed camera.

3. Mathematical Modelling

During laser welding process, heat transfer between the laser and material, mass transfer caused by evaporation, several driving forces such as recoil pressure, surface tension, and buoyancy force have been taken into account in the model. The volume-of-fluid (VOF) method was taken to handle liquid/vapor free surface. The CFD software Fluent 15.0 was used to develop the mathematical model, and a user-defined-function (UDF) file written by C language was used to realize the source terms.

The physical and thermal properties of 6056 aluminum alloy in our modelling are summarized in Table 1. The coordinate system and computational domain used in the study are shown in Figure 2.

The molten pool shape and temperature distribution were affected by variations in thermal properties [18]. Consequently, some thermophysical properties dependent on temperature were written as follows:

$$c_p\left(\mathrm{J{\cdot}kg^{-1}}\right) = \begin{cases} -0.001 \times T^2 + 1.1609 \times T + 267.71 & 300 < T \le 573 \\ 0.0009 \times T^2 - 0.3901 \times T + 514.45 & 573 < T \le 913 \\ -0.0001 \times T^2 + 0.5832 \times T + 435.14 & 913 < T \le 2740, \end{cases}$$

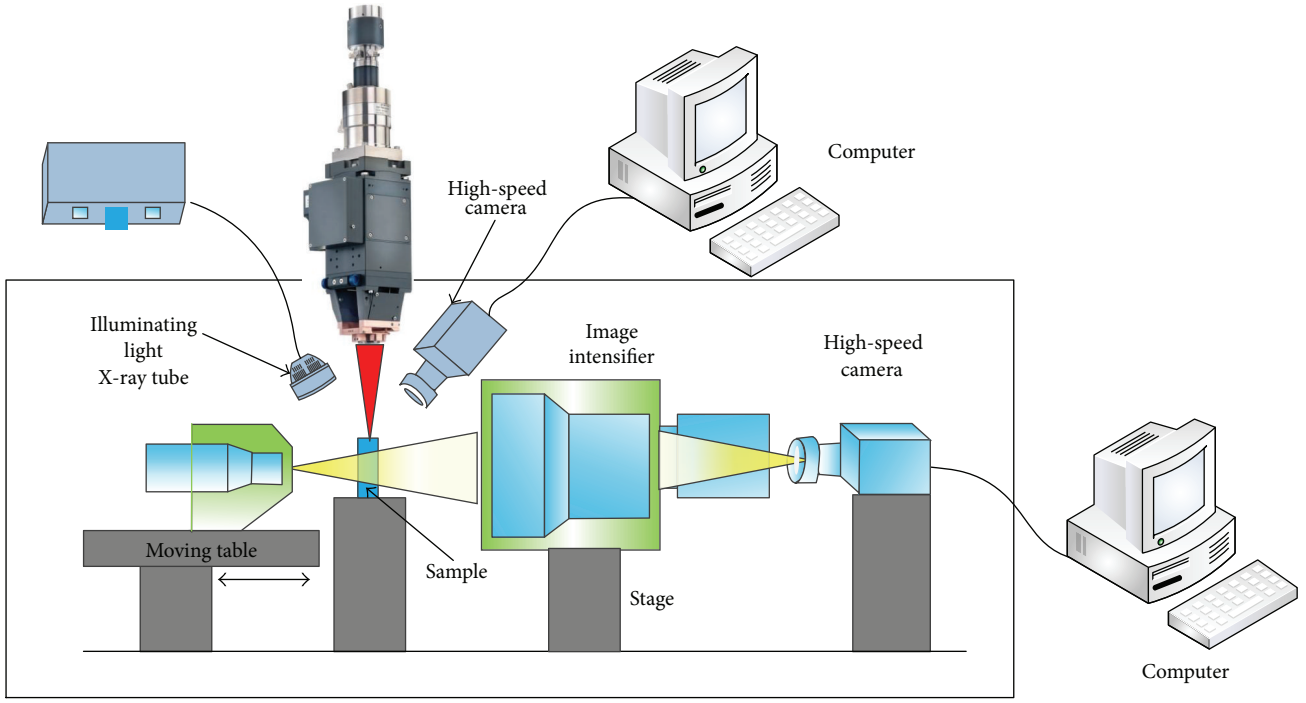

Figure 1: Welding setup of laser focusing optics, high-speed video camera, and X-ray device.

Table 1: Physical and thermal properties of 6056 aluminum alloy.

Property	Symbol	Unite	Value
Solid density	ρ_s	$kg{\cdot}m^{-3}$	2720
Liquid density	ρ_l	$kg{\cdot}m^{-3}$	2590
Solidus temperature	T_s	K	860
Liquidus temperature	T_L	K	917
Boiling temperature	T_g	K	2740
Latent heat of fusion	L_m	$J{\cdot}kg^{-1}$	3.87×10^5
Latent heat of vapor	L_v	$J{\cdot}kg^{-1}$	1.08×10^7
Thermal expansion coefficient	β_k	K^{-1}	1.92×10^{-5}
Convective heat transfer coefficient	h_0	$W{\cdot}K^{-1}{\cdot}m^{-2}$	15
Surface tension	δ_0	$N{\cdot}m^{-1}$	0.914
Surface tension gradient	A_δ	$N{\cdot}m^{-1}{\cdot}K^{-1}$	-3.5×10^{-4}
Radiation emissivity	ε	—	0.08
Ambient temperature	T_{ref}	K	300

$$k\left(\text{w}{\cdot}\text{m}^{-1}{\cdot}\text{k}^{-1}\right) = \begin{cases} -0.0001 \times T^2 - 0.0697 \times T + 95.334 & 300 < T \le 860 \\ -0.0048 \times T^2 + 9.2812 \times T - 4275.6 & 860 < T \le 917 \\ -0.00001 \times T^2 + 0.0582 \times T + 148.74 & 917 < T \le 2740, \end{cases}$$

$$u\left(\text{kg}{\cdot}\text{m}^{-1}{\cdot}\text{s}^{-1}\right) = \begin{cases} 1 \times 10^{-7} \times T^2 - 0.0002 \times T + 0.1202 & 897 < T \le 937 \\ 2 \times 10^{-11} \times T^2 - 5 \times 10^{-7} \times T + 0.0038 & 937 < T \le 2650 \\ -6 \times 10^{-8} \times T^2 + 0.0003 \times T - 0.4151 & 2650 < T \le 2720. \end{cases} \quad (1)$$

In building the model, the following assumptions and simplifications were considered. The assumptions were as follows: (1) the effect of shielding gas on welding process is ignored; (2) the flow pattern of weld pool is assumed to be laminar, and incompressible; and (3) the surface of weld pool is flat. (4) The initial temperature for workpiece is at 300 K. (5) The thermophysics material properties are constant except for specific heat, thermal conductivity, and dynamic viscosity.

3.1. Governing Equations and Boundary Conditions. The domain around the welding beam was divided into fine cells in the size of 0.1 mm, and there were 384000 cells in all, as shown in Figure 3.

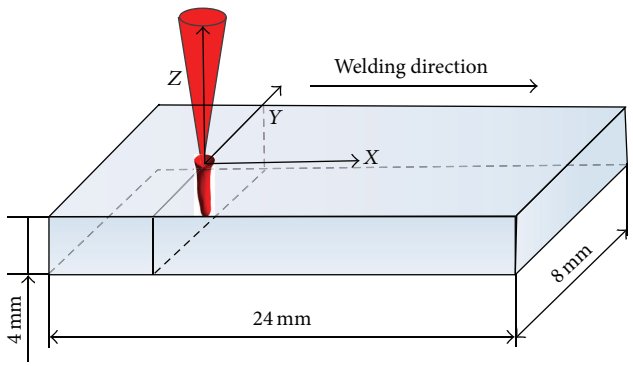

Figure 2: The schematic of the simulation domain.

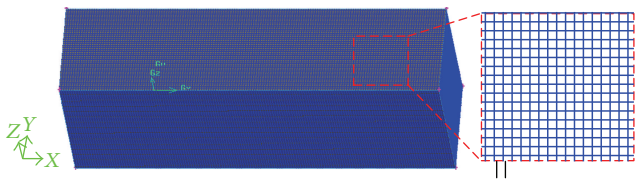

Figure 3: The mesh used in the simulation.

In the case of multiphase fluids, the governing equations were composed of continuity, energy, and momentum [19].

The continuity equation is described as

$$\frac{\partial(\rho)}{\partial t} + \frac{\partial(\rho u)}{\partial x} + \frac{\partial(\rho v)}{\partial y} + \frac{\partial(\rho w)}{\partial z} + S_m = 0. \tag{2}$$

The energy equation is described as

$$\frac{\partial(\rho H)}{\partial t} + \frac{\partial(\rho u H)}{\partial x} + \frac{\partial(\rho v H)}{\partial y} + \frac{\partial(\rho w H)}{\partial z} = \frac{\partial}{\partial x}\left(k\frac{\partial T}{\partial x}\right) + \frac{\partial}{\partial y}\left(k\frac{\partial T}{\partial y}\right) + \frac{\partial}{\partial yz}\left(k\frac{\partial T}{\partial z}\right) + S_H. \tag{3}$$

The momentum equations along different axes are described as

$$\frac{\partial(\rho u)}{\partial t} + \frac{\partial(\rho u u)}{\partial x} + \frac{\partial(\rho u v)}{\partial y} + \frac{\partial(\rho u w)}{\partial z} = \frac{\partial}{\partial x}\left(\mu\frac{\partial u}{\partial x}\right) + \frac{\partial}{\partial y}\left(\mu\frac{\partial u}{\partial y}\right) + \frac{\partial}{\partial z}\left(\mu\frac{\partial u}{\partial z}\right) - \frac{\partial P}{\partial x} + S_x,$$

$$\frac{\partial(\rho v)}{\partial t} + \frac{\partial(\rho u v)}{\partial x} + \frac{\partial(\rho v v)}{\partial y} + \frac{\partial(\rho v w)}{\partial z} = \frac{\partial}{\partial x}\left(\mu\frac{\partial v}{\partial x}\right) + \frac{\partial}{\partial y}\left(\mu\frac{\partial v}{\partial y}\right) + \frac{\partial}{\partial z}\left(\mu\frac{\partial v}{\partial z}\right) - \frac{\partial P}{\partial y} + S_y,$$

$$\frac{\partial(\rho w)}{\partial t} + \frac{\partial(\rho u w)}{\partial x} + \frac{\partial(\rho v w)}{\partial y} + \frac{\partial(\rho w w)}{\partial z} = \frac{\partial}{\partial x}\left(\mu\frac{\partial w}{\partial x}\right) + \frac{\partial}{\partial y}\left(\mu\frac{\partial w}{\partial y}\right) + \frac{\partial}{\partial z}\left(\mu\frac{\partial w}{\partial z}\right) - \frac{\partial P}{\partial z} + S_z, \tag{4}$$

where u, v, and w denote different components of velocity; ρ, P, H, k, and μ mean the density, pressure, enthalpy, thermal conductivity, and viscosity, respectively. S_m, S_x, S_y, S_z, and S_H indicate the source terms of the continuity equation, momentum equations, and energy equation.

Boundary conditions are expressed as in [20].

At top free surface inside the keyhole, the temperature dependent Marangoni shear stress on the free surface is given as

$$-u\frac{\partial u}{\partial z} = \frac{\partial\sigma}{\partial T}\frac{\partial T}{\partial x},$$
$$-u\frac{\partial v}{\partial z} = \frac{\partial\sigma}{\partial T}\frac{\partial T}{\partial y}, \tag{5}$$

where $\partial\sigma/\partial T$ is the temperature coefficient of surface tension.

In the solid region,

$$u = u_w,$$
$$v = 0, \tag{6}$$
$$w = 0,$$

where u_w is the velocity of workpiece along positive x-axis.

Along the longitudinal section plane of symmetry ($y = 0$), the boundary conditions for the velocity components are defined as

$$\frac{\partial T}{\partial y} = 0,$$
$$\frac{\partial u}{\partial y} = 0,$$
$$\frac{\partial w}{\partial y} = 0, \tag{7}$$
$$v = 0.$$

3.2. Laser Heat Source Model. Because the keyhole is filled with plasma, invert Bremsstrahlung absorption of laser energy is considered. Consequently, the model is a coupled cylinder volume heat source with energy density exponential decay in the direction of keyhole depth and Gaussian distribution in a certain height, as shown in Figure 4. Surface heat flux q_s and volumetric heat generation rate q_v are described by the following equations [21]:

$$q_s = \frac{3\chi_s P}{\pi r_s^2} e^{-3[(x-vt)^2+(y-vt)^2]/r_s^2}$$
$$q_v = \frac{3\chi_v \beta P}{\pi r_s^2\left(1-e^{-\beta T}\right)} e^{-3[(x-vt)^2+(y-vt)^2]/r_s^2} e^{-\beta(z-z_0)}, \tag{8}$$

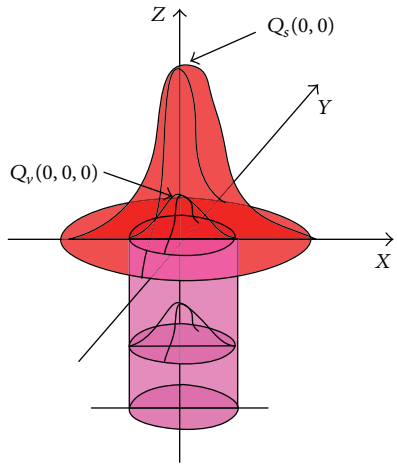

Figure 4: Schematic presentation of heat source model for laser welding.

where P is the laser power, v is the welding speed, t is the current time of laser welding, and parameters χ_s and χ_v are the fractions of heat deposited in the surface heat source and volumetric heat source, respectively. Parameter r_s is the effective radius of surface heat flux. Parameter β is the attenuation parameter in the direction of keyhole depth.

3.3. Driving Force. The recoil pressure is the crucial force for keyhole forming, by driving liquid flow in the molten pool. The following model is used in this paper, which is related to the wall temperature of the keyhole [22]:

$$P_r = AB_0T_s^{-1/2} \exp\left(-\frac{U}{T_s}\right), \tag{9}$$

where A is a numerical coefficient which is equal to 0.55 [23], and B_0 is the vaporization constant.

The surface tension of the aluminum alloy decreases with an increase in the temperature. The surface tension can be expressed as a linear function of temperature:

$$\delta(T) = \delta_0 + A_\delta(T - T_m), \tag{10}$$

where δ_0 is the surface tension of pure metal at the melting point, A_δ is the temperature coefficient of surface tension, and T_m is the melting point of the workpiece.

In the molten pool, buoyancy force (body force) can be expressed as in (11) by using the Boussinesq approximation, where only the effect of temperature difference is considered:

$$F_b = \rho g\beta(T - T_m), \tag{11}$$

where g is the gravity and β is the thermal expansion coefficient of the workpiece.

4. Results and Discussion

4.1. Melt Flows inside Molten Pools at Different Welding Speeds. The melt flows inside the molten pool were observed by utilizing X-ray transmission imaging system during laser welding of aluminum alloy plate with W particles at the laser power of 4 kW and the different welding speeds of 50 mm/s and 133 mm/s. The observation results were shown in Figure 5. The observed diffusion process of W particles showed that the molten metal on the rear molten pool had significantly different flow trends at different welding speeds. As shown in Figure 5(a), when the welding speed was 50 mm/s, W particle on the front keyhole wall at the upper part of keyhole was flowing up and flowing down to the rear molten pool immediately; W particle on the middle depth was flowing back and down, forming a strong eddy in the rear part of a keyhole; and W particle on the bottom depth was flowing toward the rear-bottom part of the molten pool under the effect of gravity and the effect of recoil pressure on the bottom of a blind keyhole. On the other hand, as seen in Figure 5(b), when the welding speed was 133 mm/s, W particle on the front keyhole wall at the upper part of keyhole was flowing up and flowing toward the rear molten pool stably, which was different from that at 50 mm/s welding speed; W particle on the middle depth was flowing up quickly to the surface of molten pool; and W particle on the bottom depth showed similar flow patterns of the molten pool as those during 50 mm/s welding speed.

From the observation results, the molten pool dynamics corresponding to the observed flow patterns of the molten pools during laser welding at the speeds of 50 mm/s and 133 mm/s were schematically illustrated in Figure 6(a). The melt flows of molten pools of numerical simulation results at 50 mm/s and 133 mm/s were shown in Figure 6(b). As shown in Figure 6, the flow patterns of the molten pools of numerical simulation results showed a similar tendency with the experimental results, and thus the process models of laser welding could be verified by experimental results. As seen in Figure 6(b), at the speed of 50 mm/s, the melt metal in the rear part of the molten pool flowed back toward the keyhole, which could explain the experimental results that W particle at the upper part of keyhole was flowing up and flowing down to the rear molten pool immediately. As seen in Figure 6(b), at the speed of 133 mm/s, the molten layer of the rear part of keyhole flowing up and toward the rear molten pool, and therefore W particle at the upper part of the keyhole could flow toward the rear molten pool stably.

At the speed of 50 mm/s, comparisons between the simulated molten pool shape and its predictions with the results of high-speed video imaging were shown in Figure 7. Figure 7(a) showed a top surface view of the molten pool and a keyhole observed using high-speed video. In this picture, a red region represented the shape of the molten pool and a red round shape at the front of molten pool was a keyhole opening. The comparison with Figure 7(b) showed that the predicted molten pool compared well with the experimentally measured one, and therefore it further verified the effectiveness of the model during laser welding of aluminum alloy.

As we knew, the flow dynamics in the molten pool had great relationship with driving forces such as recoil pressure, surface tension, buoyancy force, and gravity. From (4), it could be found that recoil pressure, surface tension, and buoyancy force were influenced by temperatures of the

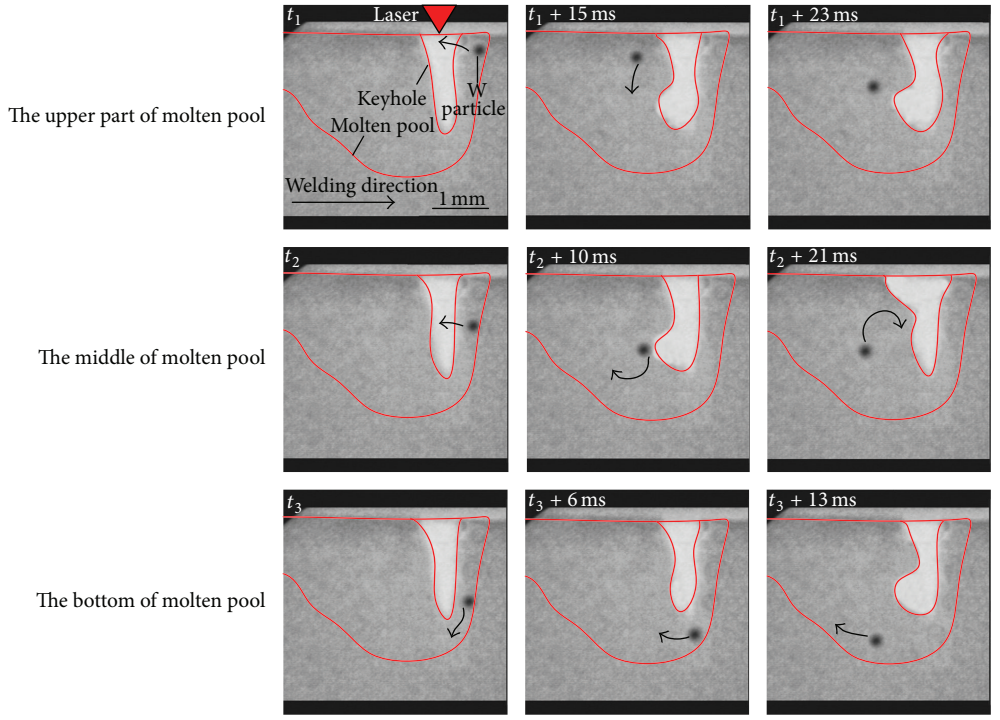

(a) Welding speed: 50 mm/s

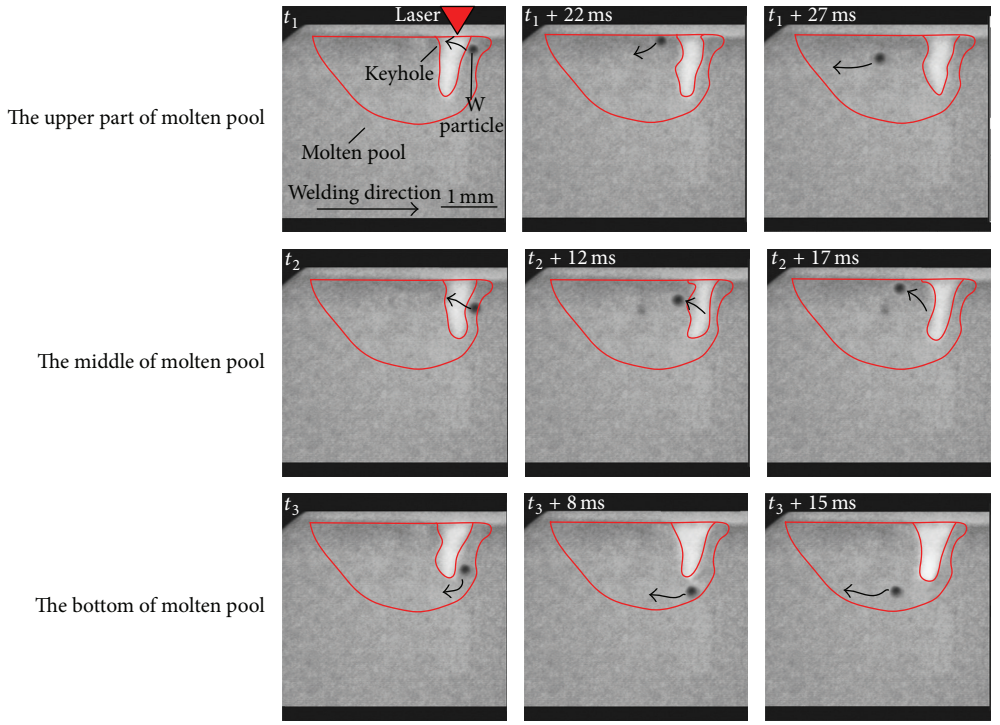

(b) Welding speed: 133 mm/s

Figure 5: Microfocused X-ray transmission in situ observation images of melt flows inside molten pools during laser welding at different speeds.

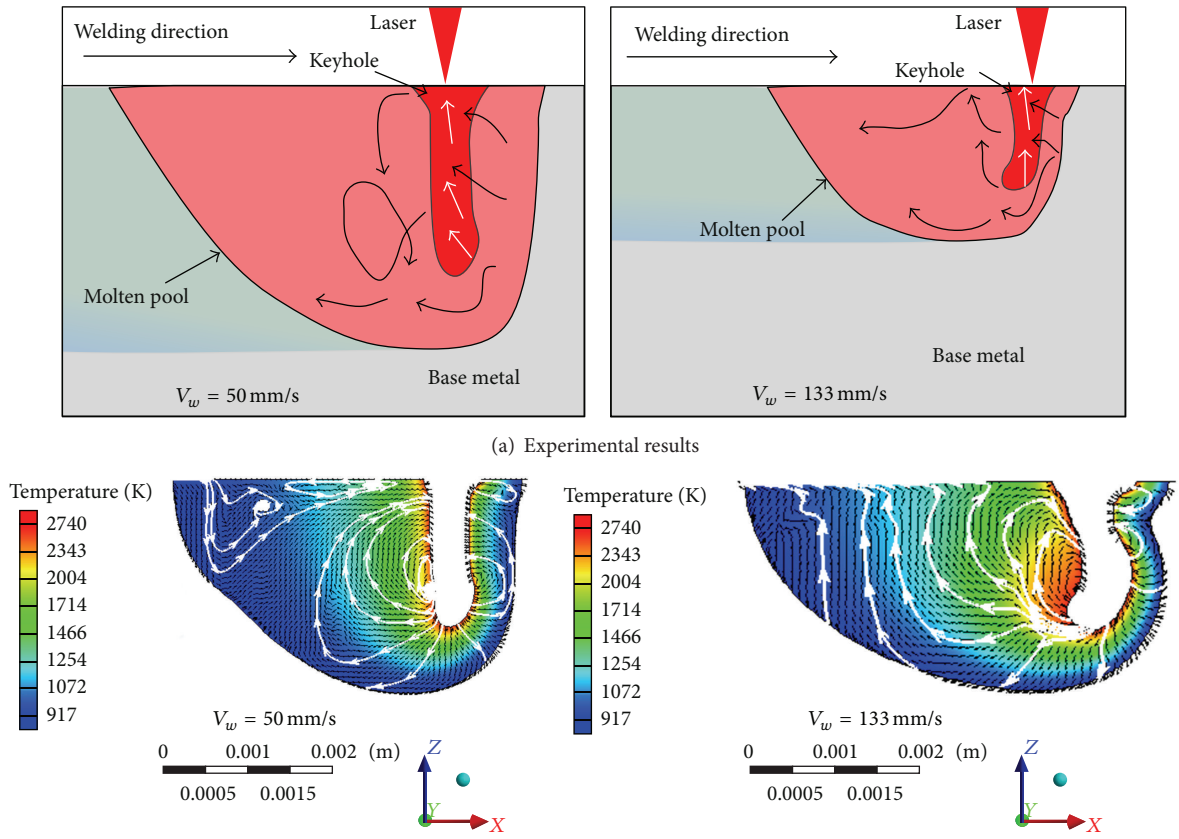

Figure 6: Melt flows inside molten pools during laser welding at different speeds.

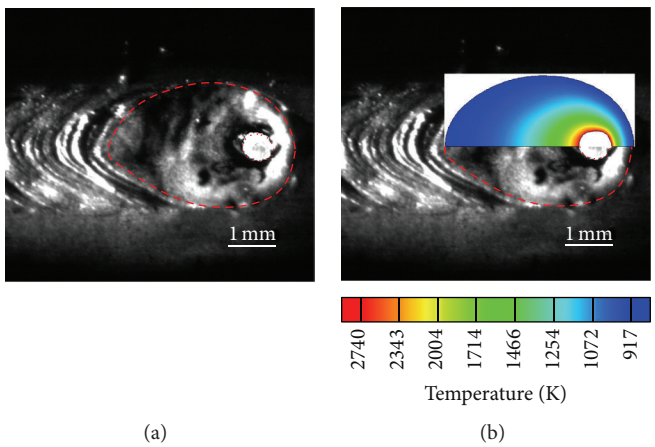

Figure 7: Top surface views of predicted weld pool shape. (a) Experimentally observed molten pool and (b) comparison of molten pool obtained by experiment and simulation.

molten pool. Consequently, it was necessary to analyze the correlation between temperature gradient and melt flow of molten pool in laser welding of aluminum alloy. It was reported that the motion of metallic vapor bubble was exceedingly similar to the molten pool flow [10]. Moreover, the motion paths of bubble were divided into two kinds: some bubbles floated up and disappeared from the top surface and the other ones floated toward the rear molten pool were captured or trapped by the solidifying interface of the weld metal [5]. As the welding speeds gradually increased, the weld penetration gradually decreased, and thus the length of line AB was different. Figure 8 indicated that each point corresponded to temperature value along AB direction during laser welding at different speeds. It was found that the

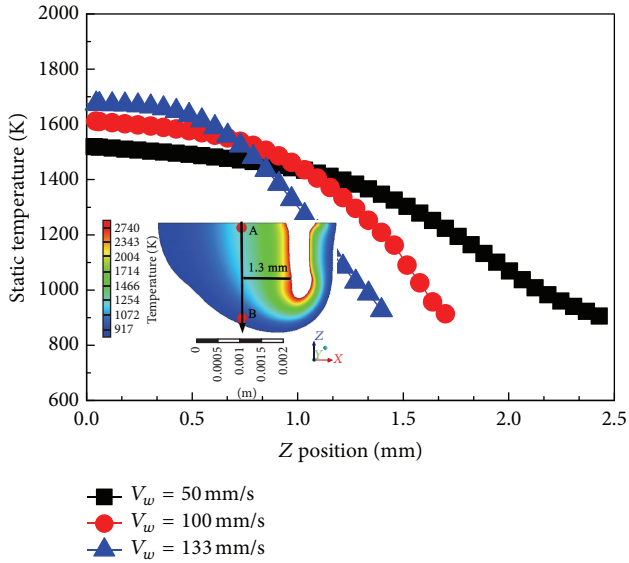

FIGURE 8: Static temperature profiles along line AB during laser welding at different speeds.

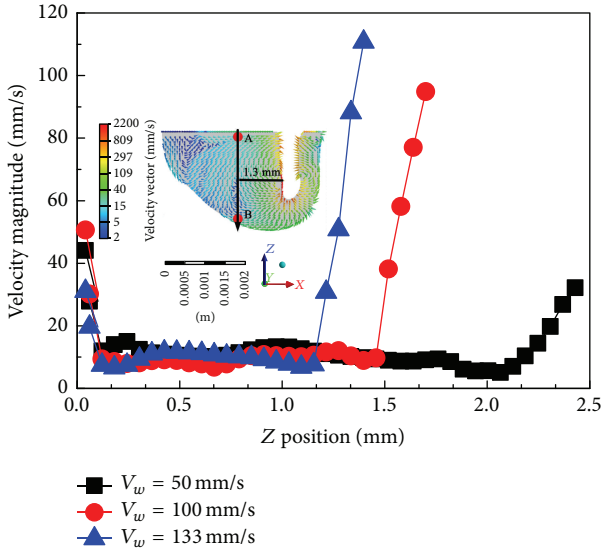

FIGURE 9: Velocity magnitude profiles along line AB during laser welding at different speeds.

temperature along the direction of weld penetration gradually decreased. In keyhole laser welding, the hydrodynamics of molten pool generated had always appeared to be very complex. The melt flow of molten pool influenced heat and mass transfer in the weld. In the quasisteady stage of laser welding process, the laser energy coupling efficiency and the shape of molten pool surface changed periodically. As shown in Figure 9, as the welding speeds increased, the flow velocity at the bottom of molten pool increased. And the flow trend that liquid metal of molten pool from the high-temperature area at the bottom of the keyhole to the low-temperature area at the top of molten pool increased as welding speed increased, as shown in Table 2. Therefore, the temperature at the surface of the melt pool (point A) in Figure 8 increased with increasing welding speeds. Figure 9 showed the velocity magnitude profile along line AB at different welding speeds. It was found that, in the rear part of molten pool produced by laser welding, the maximum flow velocity was located at the bottom of molten pool.

Table 2 showed the temperature profile and flow pattern of the molten pool corresponding to temperature gradient of point A and point B and flow velocity of point B with different welding speeds. The flow patterns of molten pool were demonstrated by the arrowed curves. The results showed that the melt metal in the rear molten pool caused by welding speeds had significantly different flow trends. The top view of the molten pool showed that at 50 mm/s the melt metal flowed to the rear from the front of the molten pool; then the backflow caused by the Marangoni surface tension gradient was formed at the rear of the molten pool that was consistent with reports by Matsunawa et al. [24] Kaplan et al. [25] took the attitude that the fluctuation broke the stability of the molten pool. As the welding speeds gradually increased to 100 mm/s and 133 mm/s, the melt metal directly flowed to the rear from the front of the molten pool, and the backflow disappeared.

From the longitudinal view of the molten pool, it was found that the melt metal at the bottom of the keyhole flowed downwards, which was caused by the recoil pressure of a laser beam, maintaining the keyhole depth. At 50 mm/s, in the rear part of molten pool, the clockwise eddy caused by the effect of Marangoni surface tension gradient was formed. It was found that as the welding speeds gradually increased, temperature gradient of point A and point B gradually increased, the flow velocity at the bottom of the molten pool also increased, and the flowing trend of molten layer of the rear part of keyhole flowing up and toward the rear molten pool gradually increased, and it meant that the molten pool behavior was relatively stable. In the rear part of the molten pool, when the welding speeds increased from 50 mm/s to 133 mm/s, the temperature gradient of point A and point B increased from 252 K/mm to 552 K/mm, and the flow velocity at the bottom of molten pool increased from 32 mm/s to 111 mm/s.

4.2. Melt Flows inside Molten Pool with Different Preheating Temperatures. In order to further study the influence of the temperature gradient of point A and point B on melt flow inside the molten pool. The flow behavior of the molten pool by preheating temperature was analyzed. Figure 10 showed the static temperature profile of line AB along the direction of weld penetration at different preheating temperatures. It was found that as the preheating temperature gradually increased, the static temperature of the same position in the molten pool gradually increased. The velocity magnitude profiles along line AB at different preheating temperatures were shown in Figure 11. It was found that, in the rear part of molten pool produced by laser welding, the maximum flow velocity was located at the bottom of molten pool. As the preheating temperatures gradually increased, the velocity of melt flows at the bottom of the molten pool gradually increased.

Table 3 showed the temperature profile and flow pattern of the molten pool corresponding to temperature gradient of

Table 2: Temperature profiles and flow patterns of molten pools corresponding to temperature gradient of point A and point B and flow velocity of point B at different welding speeds and 4 kW laser power.

Welding speeds	Top view	Longitudinal section view	Temperature gradient of point A and point B	Flow velocity of point B
V_w = 50 mm/s	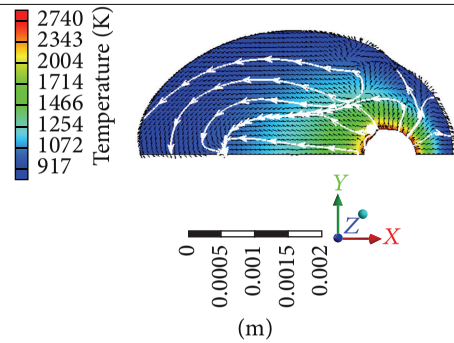	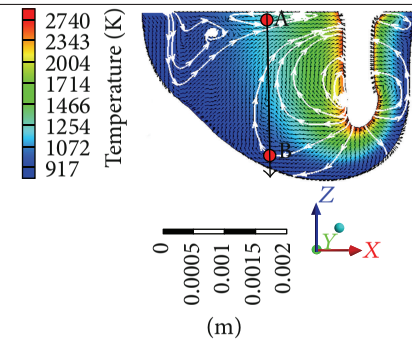	252 K/mm	32 mm/s
V_w = 100 mm/s	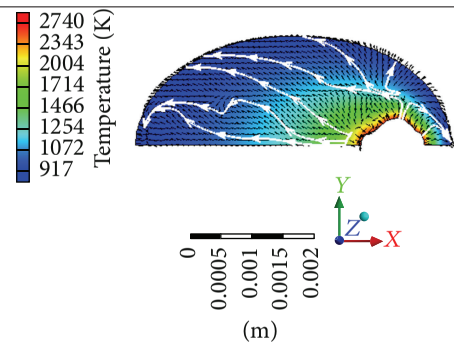	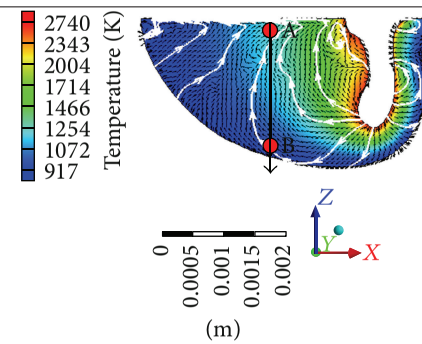	421 K/mm	95 mm/s
V_w = 133 mm/s	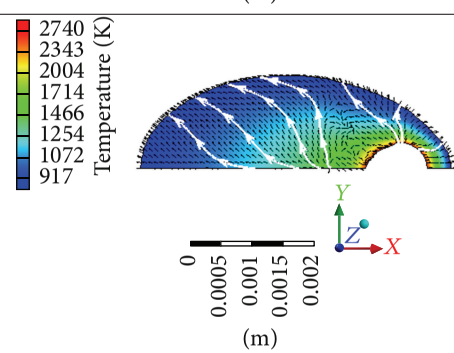	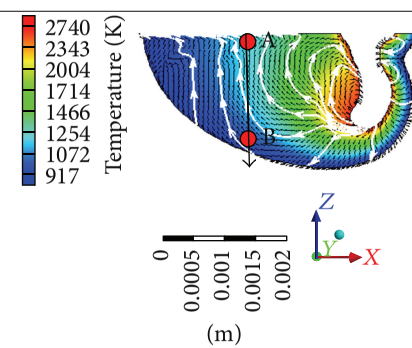	552 K/mm	111 mm/s

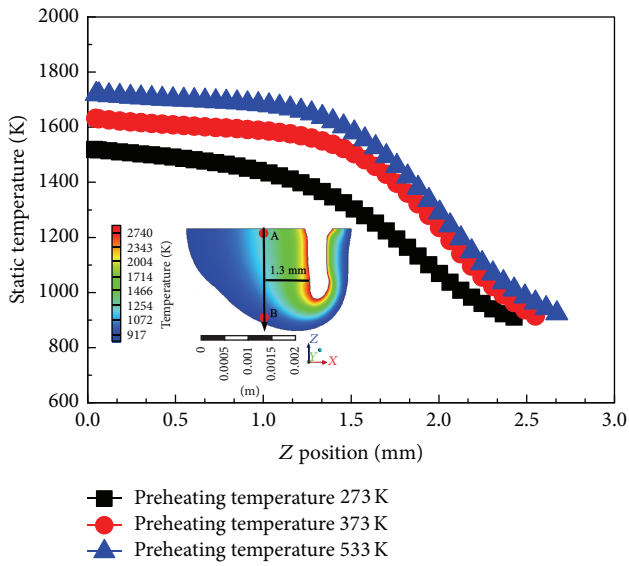

Figure 10: Static temperature profiles along line AB at different preheating temperatures.

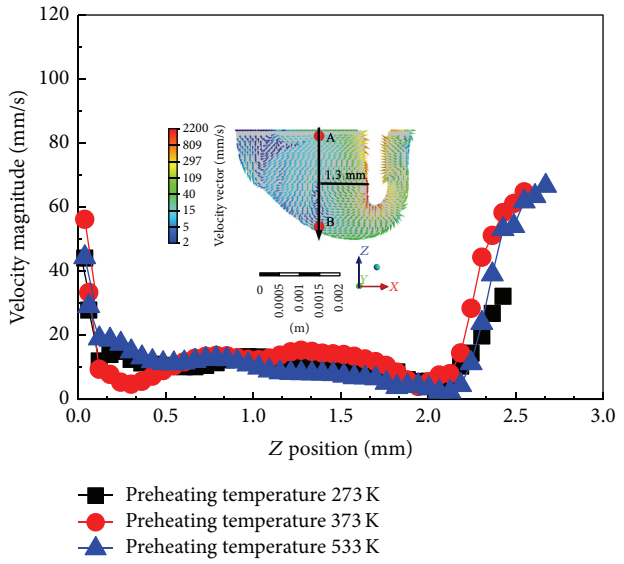

Figure 11: Velocity magnitude profiles along line AB at different preheating temperatures.

point A and point B and flow velocity of point B at different preheating temperatures when welding speed was 50 mm/s and laser power was 4 kW. The top view of the molten pool showed that as the preheating temperature gradually increased, the backflow on the molten pool surface caused by the Marangoni surface tension gradient gradually increased and the length and width of molten pool gradually increased. On the longitudinal molten pool, it was found that as preheating temperature gradually increased, the temperature gradient of point A and point B along the direction of weld penetration gradually increased and the flow velocity at the bottom of the molten pool also increased. In the rear part of the molten pool, when preheating temperatures increased

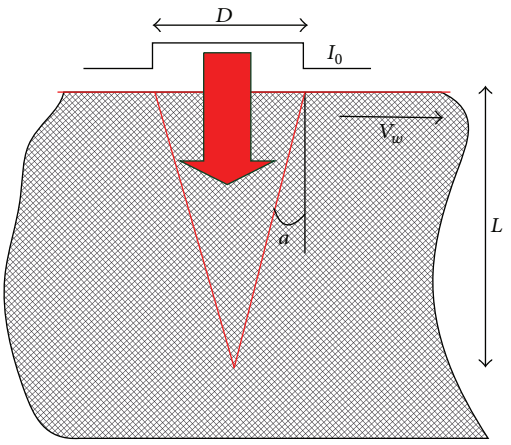

Figure 12: Scheme of the longitudinal section of a keyhole.

from 273 K to 533 K, the temperature gradient of point A and point B increased from 252 K/mm to 298 K/mm, and the flow velocity at the bottom of molten pool increased from 32 mm/s to 70 mm/s. However, the flow pattern of the molten pool caused by preheating temperature was not significantly changed.

In keyhole mode laser welding, the temperature gradient along the direction of weld penetration could be caused by welding speeds and preheating temperature. However, melt flows of the molten pool corresponding to temperature gradient were significantly different at different welding speeds and preheating temperatures. In addition, as the welding speed gradually increased, the vortices existed in the rear molten pool disappeared and the tendency of the melt upward movement increased. This phenomenon was beneficial to improving the stability of molten pool and reducing the porosity of weld bead [7]. As the preheating temperatures gradually increased, the vortices still existed in the rear molten pool, and the flow pattern of the molten pool was not significantly changed. Consequently, compared with the increase of the preheating temperature, the increase of the welding speed was more beneficial to improving the stability of molten pool.

The influence of welding speed on the stability of the molten pool was analyzed as follows. In keyhole mode laser welding, the dynamic fluctuation of the keyhole directly affected the stability of the molten pool. For a uniform incident intensity profile, a scheme of the longitudinal section of the keyhole walls with corresponding notations was shown in Figure 12.

In keyhole mode laser welding, penetration depth L could be expressed as in the following equation [26]:

$$L \approx \frac{kI_0A_0D}{V_w} = \frac{(4A_0k/\pi)\,P}{(DV_w)}, \tag{12}$$

where P was the incident laser power, I_0 was the incident laser intensity, A_0 was the absorptivity under normal incidence, D was the keyhole diameter, and k was representative of some energy balance of the process that depended mainly

Table 3: Temperature profiles and flow patterns of molten pools corresponding to temperature gradient of point A and point B and flow velocities of point B at different preheating temperatures during laser welding of aluminum alloy at 50 mm/s welding speed and 4 kW laser power.

Preheating temperature	Top view	Longitudinal section view	Temperature gradient of point A and point B	Flow velocity of point B
273 K (ambient temperature)	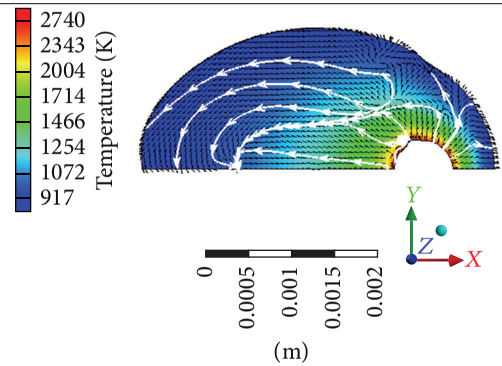	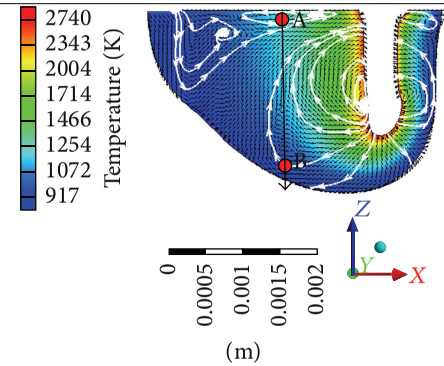	252 K/mm	32 mm/s
373 K	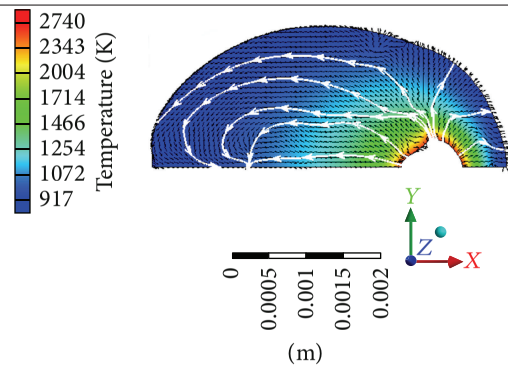	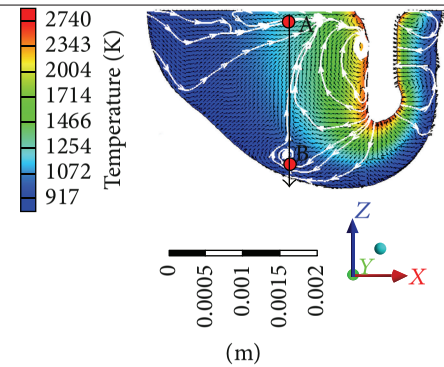	279 K/mm	65 mm/s
533 K	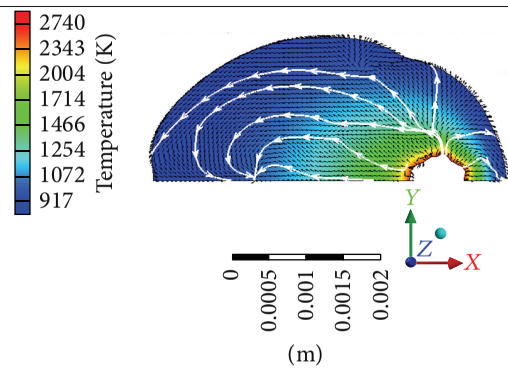	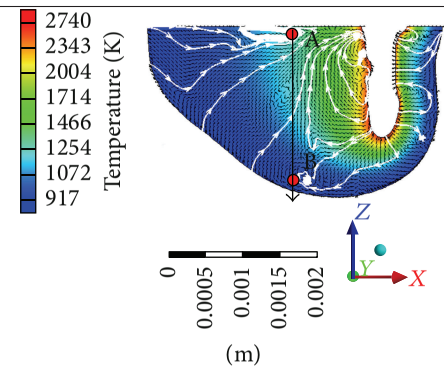	298 K/mm	70 mm/s

on the workpiece material. Equation (12) showed that the penetration depth scaled as $1/V_w$.

Absorbed intensity I_{abs} on the keyhole front, which was given as in

$$I_{\text{abs}} = I_0 A_0 \sin a = \frac{V_w}{k}, \tag{13}$$

where a was keyhole front wall inclination. It was found that the absorbed intensity on the keyhole front was totally independent of the incident intensity; it only depended on the welding speeds.

During laser penetration welding process, factors influencing the dynamic behavior of molten pool mainly included surface tension which would closed keyhole and recoil pressure which helped maintain keyhole [16]. The keyhole would be maintained open, if the excess of recoil pressure P_{evap} over ambient pressure P_a counterbalanced surface tension pressure $P_s = 2\sigma/D$ inside the keyhole [27]. As this opening pressure was increasing with the absorbed intensity, (13) indicated that, for low welding speeds, the absorbed intensity was rather small, and this excess of recoil pressure became lower than the characteristic keyhole closing pressure controlled by surface tension [26]. Therefore, for these conditions, the keyhole could not be stationary; it closed itself quite periodically and was continuously reopened, as in a drilling process, by the continuous incoming incident laser beam. As shown in Table 2, as the welding speeds increased, keyhole front wall inclination increased. Therefore, the absorbed intensity on the keyhole front wall also increased as well as the recoil pressure. The recoil pressure could keep the keyhole open, and the stability of the molten pool was improved.

5. Conclusions

By using the X-ray transmission imaging system and the numerical simulation, the correlation between temperature gradient along the direction of weld penetration and melt flow in the rear part of molten pool was studied during laser welding of aluminum alloy at different welding speeds and preheating temperatures. The following conclusions could be summarized from the results of the present work:

(1) The melt metal in the rear molten pool caused by welding speeds had significantly different flow trends. As the welding speed (≥100 mm/s) gradually increased, the vortices existed in the rear molten pool disappeared, the tendency of the melt upward movement increased. Compared with welding speeds, and the flow pattern of molten pool caused by preheating temperature was not significantly changed.

(2) In the rear part of the molten pool produced by laser welding, the maximum flow velocity was located at the bottom of the molten pool. The flow velocity at the bottom of the molten pool caused by welding speed (133 mm/s) was higher than that caused by preheating temperature (533 K). The flow velocity at the bottom of the molten pool increased from 32 mm/s to 111 mm/s, as the welding speed increased from 50 mm/s to 133 mm/s, while the flow velocity at the bottom of the molten pool was 70 mm/s at the preheating temperature of 533 K and welding speed of 50 mm/s.

(3) The temperature gradient of point A and point B along the direction of weld penetration caused by welding speed (133 mm/s) was higher than that caused by preheating temperature (533 K). In the rear part of molten pool, the temperature gradient increased from 252 K/mm to 552 K/mm as the welding speed increased from 50 mm/s to 133 mm/s, while the temperature gradient was 298 K/mm at the preheating temperature of 533 K and the welding speed of 50 mm/s.

(4) In keyhole mode laser welding, the temperature gradient along the direction of weld penetration could be caused by welding speeds and preheating temperature. However, melt flows of the molten pool corresponding to temperature gradient were significantly different at different welding speeds and preheating temperatures.

(5) Compared with the increase of the preheating temperature, the increase of the welding speed was more beneficial to improving the stability of molten pool. That is because as the welding speed increased, the absorbed intensity on the keyhole front wall increased as well as the recoil pressure. Consequently, the recoil pressure could keep the keyhole open, and the stability of the molten pool was improved.

(6) The results of the proposed three-dimensional model were validated by experimental observation results obtained with the high-speed camera and the X-ray transmission imaging system and qualified the agreement between observed X-ray images and numerical simulation results by comparing the flow patterns and sizes of the melt pool at different welding speeds.

Competing Interests

The authors declare that they have no competing interests.

Acknowledgments

This work is finically supported by the National Natural Science Foundation of China (no. 51175115). Also, the authors wish to express their sincere thanks to Dr. Guolong Ma for useful technical discussions and support during the course of this project.

References

[1] A. C. Oliveira, R. H. M. Siqueira, R. Riva, and M. S. F. Lima, "One-sided laser beam welding of autogenous T-joints for 6013-T4 aluminium alloy," *Materials and Design*, vol. 65, pp. 726–736, 2015.

[2] D. Narsimhachary, R. N. Bathe, G. Padmanabham, and A. Basu, "Influence of temperature profile during laser welding of aluminum alloy 6061 T6 on microstructure and mechanical properties," *Materials and Manufacturing Processes*, vol. 29, no. 8, pp. 948–953, 2014.

[3] F. Caiazzo, V. Alfieri, F. Cardaropoli, and V. Sergi, "Butt autogenous laser welding of AA 2024 aluminium alloy thin sheets with a Yb:YAG disk laser," *International Journal of Advanced Manufacturing Technology*, vol. 67, no. 9–12, pp. 2157–2169, 2013.

[4] S. Tsukamoto, "High speed imaging technique part 2—high speed imaging of power beam welding phenomena," *Science and Technology of Welding and Joining*, vol. 16, no. 1, pp. 44–55, 2011.

[5] S. Katayama and A. Matsunawa, "Microfocused X-ray transmission real-time observation of laser welding phenomena," *Welding International*, vol. 16, no. 6, pp. 425–431, 2002.

[6] A. Matsunawa, "Problems and solutions in deep penetration laser welding," *Science and Technology of Welding and Joining*, vol. 6, no. 6, pp. 351–354, 2001.

[7] Y. Kawahito, M. Mizutani, and S. Katayama, "Elucidation of high-power fibre laser welding phenomena of stainless steel and effect of factors on weld geometry," *Journal of Physics D: Applied Physics*, vol. 40, no. 19, pp. 5854–5859, 2007.

[8] Y. Kawahito, M. Mizutani, and S. Katayama, "High quality welding of stainless steel with 10 kW high power fibre laser," *Science and Technology of Welding and Joining*, vol. 14, no. 4, pp. 288–294, 2009.

[9] S. Li, G. Chen, S. Katayama, and Y. Zhang, "Relationship between spatter formation and dynamic molten pool during high-power deep-penetration laser welding," *Applied Surface Science*, vol. 303, pp. 481–488, 2014.

[10] W. Meng, Z. Li, F. Lu, Y. Wu, J. Chen, and S. Katayama, "Porosity formation mechanism and its prevention in laser lap welding for T-joints," *Journal of Materials Processing Technology*, vol. 214, no. 8, pp. 1658–1664, 2014.

[11] B. Chang, C. Allen, J. Blackburn, P. Hilton, and D. Du, "Fluid flow characteristics and porosity behavior in full penetration laser welding of a titanium alloy," *Metallurgical and Materials Transactions B*, vol. 46, no. 2, pp. 906–918, 2015.

[12] M. Sohail, S.-W. Han, S.-J. Na, A. Gumenyuk, and M. Rethmeier, "Characteristics of weld pool behavior in laser welding with various power inputs," *Welding in the World*, vol. 58, no. 3, pp. 269–277, 2014.

[13] H. Wang, Y. Shi, and S. Gong, "Numerical simulation of laser keyhole welding processes based on control volume methods," *Journal of Physics D: Applied Physics*, vol. 39, no. 21, pp. 4722–4730, 2006.

[14] L. Zhang, J. Zhang, G. Zhang, W. Bo, and S. Gong, "An investigation on the effects of side assisting gas flow and metallic vapour jet on the stability of keyhole and molten pool during laser full-penetration welding," *Journal of Physics D: Applied Physics*, vol. 44, no. 13, Article ID 135201, 2011.

[15] M. Bachmann, V. Avilov, A. Gumenyuk, and M. Rethmeier, "About the influence of a steady magnetic field on weld pool dynamics in partial penetration high power laser beam welding of thick aluminium parts," *International Journal of Heat and Mass Transfer*, vol. 60, no. 1, pp. 309–321, 2013.

[16] L. J. Zhang, J. X. Zhang, A. Gumenyuk, M. Rethmeier, and S. J. Na, "Numerical simulation of full penetration laser welding of thick steel plate with high power high brightness laser," *Journal of Materials Processing Technology*, vol. 214, no. 8, pp. 1710–1720, 2014.

[17] K. Abderrazak, S. Bannour, H. Mhiri, G. Lepalec, and M. Autric, "Numerical and experimental study of molten pool formation during continuous laser welding of AZ91 magnesium alloy," *Computational Materials Science*, vol. 44, no. 3, pp. 858–866, 2009.

[18] S. Bannour, K. Abderrazak, H. Mhiri, and G. Le Palec, "Effects of temperature-dependent material properties and shielding gas on molten pool formation during continuous laser welding of AZ91 magnesium alloy," *Optics and Laser Technology*, vol. 44, no. 8, pp. 2459–2468, 2012.

[19] H. Zhao, W. Niu, B. Zhang, Y. Lei, M. Kodama, and T. Ishide, "Modelling of keyhole dynamics and porosity formation considering the adaptive keyhole shape and three-phase coupling during deep-penetration laser welding," *Journal of Physics D: Applied Physics*, vol. 44, no. 48, Article ID 485302, 2011.

[20] R. Wang, Y. Lei, and Y. Shi, "Numerical simulation of transient temperature field during laser keyhole welding of 304 stainless steel sheet," *Optics and Laser Technology*, vol. 43, no. 4, pp. 870–873, 2011.

[21] Y. Chen, L. Li, J. Fang, and X. Feng, "Numerical analysis of energy effect in laser-TIG hybrid welding," *Journal of Materials Science and Technology*, vol. 19, pp. 23–26, 2003.

[22] V. Semak and A. Matsunawa, "The role of recoil pressure in energy balance during laser materials processing," *Journal of Physics D: Applied Physics*, vol. 30, no. 18, pp. 2541–2552, 1997.

[23] V. V. Semak, W. D. Bragg, B. Damkroger, and S. Kempka, "Transient model for the keyhole during laser welding," *Journal of Physics D: Applied Physics*, vol. 32, no. 15, pp. L61–L64, 1999.

[24] A. Matsunawa, N. Seto, J.-D. Kim, M. Mizutani, and S. Katayama, "Dynamics of keyhole and molten pool in high-power CO_2 laser welding," in *High-Power Lasers in Manufacturing*, vol. 3888 of *Proceedings of SPIE*, pp. 34–45, Osaka, Japan, November 1999.

[25] A. F. H. Kaplan, M. Mizutani, S. Katayama, and A. Matsunawa, "Unbounded keyhole collapse and bubble formation during pulsed laser interaction with liquid zinc," *Journal of Physics D: Applied Physics*, vol. 35, no. 11, pp. 1218–1228, 2002.

[26] R. Fabbro, "Melt pool and keyhole behaviour analysis for deep penetration laser welding," *Journal of Physics D: Applied Physics*, vol. 43, no. 44, Article ID 445501, 2010.

[27] K. Hirano, R. Fabbro, and M. Muller, "Experimental determination of temperature threshold for melt surface deformation during laser interaction on iron at atmospheric pressure," *Journal of Physics D: Applied Physics*, vol. 44, no. 43, Article ID 435402, 2011.